Dependence of partially saturated polarization spectroscopy signals on pump intensity and collision rate

Joachim Walewski,[1,*] Clemens F. Kaminski,[2] Sherif F. Hanna,[3] and Robert P. Lucht[3]

[1]*Division of Combustion Physics, Lund Institute of Technology, P.O. Box 118, SE-221 00 Lund, Sweden*

[2]*Department of Chemical Engineering, University of Cambridge, Pembroke Street, Cambridge CB2 3RA, United Kingdom*

[3]*Department of Mechanical Engineering, Texas A&M University, College Station, Texas 77843-3123*

Understanding the saturation behavior of polarization-spectroscopy signals is a vital task for the development of this method as a versatile tool for quantitative detection of trace species. Recent progress in the theoretical treatment of the polarization-spectroscopy process offers the opportunity of studying its saturation behavior thoroughly. This theoretical treatment, referred to as direct numerical integration (DNI) calculations, is based on numerically demanding calculations; that is why we present a simple model that describes the curve shape of polarization spectroscopy power-dependence scans in both the saturated and the unsaturated regime. Polarization-spectroscopy-saturation curves in the copropagating beam geometry from the excitation of OH $A\ ^2\Sigma^+ - X\ ^2\Pi(0,0)$ at the $Q_2(8)$ line in a low-pressure flame were compared to both results from the DNI calculations and to our proposed analytical equation. Our simple model provides excellent fits to polarization-spectroscopy-saturation curves for absorption lines dominated by homogeneous broadening and for narrow-bandwidth excitation sources. The model does not give a good agreement with experiment for lines dominated by inhomogeneous broadening. For this case an empirical equation is proposed and investigated. Our proposed model offers a starting point for a simplification of the underlying polarization-spectroscopy theory, the complexity of which has been a major obstacle to the further development of this theory.

I. INTRODUCTION

In polarization spectroscopy (PS) either a linearly or a circularly polarized pump beam and a weak linearly polarized probe beam are crossed within a sample. If the wavelength of the beams matches a transition in the sample, the pump beam induces an optical anisotropy. This leads to a polarization-dependent complex refractive index of the sample and a consequent rotation and ellipticity of the probe beam's polarization state. This effect can be detected using crossed polarizers in the probe beam on opposite sides of the crossing point [1,2]. An overview of PS can be found in the review of Demtröder [3]. A presentation of PS in the context of combustion diagnostics has been given by Eckbreth [4].

PS is a four-wave-mixing technique in which pump photons are absorbed by the medium, inducing an aligned population at which probe photons are scattered coherently. Other common four-wave-mixing techniques are coherent anti-Stokes Raman spectroscopy and degenerate four-wave mixing (DFWM). Only two crossing beams are needed for PS and the phase-matching condition for the interaction of probe and pump beam is automatically fulfilled, which makes it a comparatively simple experimental technique. Since it provides a signal on virtually zero background one obtains excellent signal-to-noise (SN) ratios. This, together with the fact that PS is a resonant technique, makes detection of atoms and molecules in the gas phase at low densities possible.

Nyholm *et al.* demonstrated PS on minor flame species such as OH, C_2, NH_3, and CO [5–8]. The later work of Dreizler *et al.* [9] and Kaminski *et al.* [10] extended the list of detectable molecules in the gas phase with NH and N_2. These results were very promising with respect to concentration measurements of minor species in combustion processes and reacting flows.

When attempting to measure species concentrations with PS, one has to answer two main questions [5,7]: (1) How does the PS signal depend on the local collision and quenching rate in the sample? (2) How does the generated PS signal depend on the pump intensity in saturated regimes? The first question has been studied theoretically by Reichardt and Lucht [11] and Giancola *et al.* [12], and recently both theoretically and experimentally for picosecond excitation by Reichardt *et al.* [13]. The second question has to be answered if low concentrations are to be measured. As the PS signal depends on the square of the number density [2] one usually resorts to high pump intensities to compensate for a loss in signal. The experimental intensities may reach levels at which the induced anisotropy of the pumped transition saturates [14]. A merit of saturated PS is its low sensitivity to collisions and quenching when compared to both unsaturated PS and saturated laser-induced fluorescence (LIF). This has been indicated by the aforementioned theoretical studies of PS.

The objective of this work is to investigate the dependence of the PS signal on the pump intensity in partially saturated and unsaturated regimes for different collision rates. This was investigated using both experimental and theoretical methods. In the experimental part the power dependence of PS signals from OH in the copropagating beam

___

*Corresponding author.
Email address: joachim.walewski@forbrf.lth.se

geometry was recorded in a low-pressure flame for different pressures and hence for different collision rates. The saturation curves obtained were analyzed with respect to their functional dependence on the pump intensity, i.e., their shape. The experimental saturation curves were also compared with curves obtained from a model for the PS signal generation presented by Reichardt and Lucht [11] and Giancola et al. [12] (see Sec. II for a detailed discussion).

The aim of our investigation is to make PS a versatile and practical tool for concentration measurements. We therefore aim to find simple algebraic equations to describe the PS saturation behavior. The numerical model of Lucht and co-workers [11,12] is a versatile tool allowing a parametric study of PS signals over a wide range of, e.g., pump intensities, but it does not provide a mathematically tractable set of equations. We propose a generic equation based on a simple model for the PS-signal-generation process. In this model PS is described as coherent forward scattering of probe photons [15]. The generation of the anisotropically distributed population, at which the probe photons are scattered, is described as the optical pumping of a two-level system. This simple model was fitted both to the theoretical and the experimental saturation curves in order to investigate its validity.

The experimental saturation curve shape is found to be in good agreement with results from the model of Lucht and co-workers [11,12] and our simple saturation model. The proposed model offers, due to its inherent simplicity, the possibility of parametrical studies of the PS-generation and -saturation process. It also provides a simple means to correct PS signals for changes in the laser intensity.

In a forthcoming paper we will present results from relative concentration measurements using PS of OH and apply the equation proposed in this work [16].

The outline of the remainder of the paper is organized as follows. In the theory section an overview of different PS theories is given with respect to their treatment of saturation effects. After this the model of Lucht and co-workers [11,12] is discussed and the proposed simple model for the dependence of PS signals in unsaturated and saturated regimes is presented. Thereafter, the experimental setup is described followed by a discussion of the results. Finally, the results are summarized and the impact of our findings on the further development of PS is outlined.

II. THEORY

Wieman and Hänsch were the first to demonstrate PS and to derive a theory for PS in the counterpropagating geometry [1]. Their theory was derived using results from the saturation-spectroscopy theory. It is based on the assumption of low pump intensities to allow the use of a perturbation treatment of the quantum-mechanical Liouville equation [17]. This description was reviewed in a later publication by Teets et al. [2]. In their description it is assumed that the anisotropy in the excited state, which is induced by optical pumping, is negligible. The assumption of zero anisotropy in the excited state implies that the upper-state population is destroyed at a much higher rate than the pump rate, there-fore, saturation effects cannot be described with this theory.

More recent approaches to a theory of PS were presented by Nakayama [15] and by Suvernev and co-workers [18–20] and Reichardt et al. [13]. Nakayama solved the Liouville equation assuming steady state and only considering the induced anisotropy in the ground state, which is similar to the treatment of Teets et al.; Suvernev and co-workers and Reichardt et al. used a perturbation approach. The latter account for the excited-state anisotropy and collisional relaxation in ground and excited states, which was not the case for the theory of Teets et al., but they are not valid for pump intensities in the saturated regime.

Although a PS theory accounting for saturation has long been recognized to be a crucial step towards a quantitative theory [9,11,12,14,19], few attempts have been made to develop such a theory. The main reasons for this are as follows. A realistic PS theory has to treat all degenerate magnetic sublevels in the ground and excited states that are coupled by the pump laser. In practical cases the density matrix of the system can therefore be extremely large. To allow for high pump intensities one has to deal with an appreciable population in the excited state, prohibiting the use of a perturbation-theory approach. Finally, the finite-laser linewidth and the multiaxial mode structure of practical lasers have to be taken into account.

Reichardt and Lucht [11] and later Giancola et al. [12] attacked these problem by direct numerical integration (DNI) of the Liouville equation. By using this approach they were not limited to assumptions on collision rates, laser intensities, and the axial-mode profile. To our knowledge, it is up to now the only approach dealing with PS-saturation effects, and it was therefore used in this work for comparison of experimental PS-saturation curves with predictions from theory.

A. Solution of the quantum-mechanical Liouville equation with DNI

Polarization-spectroscopy calculations were performed in this work by direct numerical integration of the Liouville equation as discussed in detail by Reichardt and Lucht [11] and Giancola et al. [12]. The collisional model and the laser model together with the important features of the DNI code are described below.

1. Collisional models

The numerical-modeling approach outlined by Giancola et al. [12] is adopted. Laser-coupled upper states (J_b, M_b) and lower states (J_a, M_a) are strongly coupled to other rotational levels in the upper and lower vibration-rotation manifold. Groups of rotational levels coupled to the laser-coupled levels are referred to as bath levels. In the following analysis, laser-coupled lower and upper levels are designated 1 and 2, whereas upper and lower bath levels are labeled 3 and 4.

The population of level 1 prior to laser excitation is assumed to be 1% of the total population, distributed equally among the $2J_a + 1$ degenerate magnetic sublevels. It is assumed that 99% of the initial population is in level 4. Population transfer between levels 1 and 4 is caused by collisions.

Relative rates of rotational transfer from level 1 to 4 and vice versa are determined by the principle of detailed balancing $n_1^0 \Gamma_{14} = n_4^0 \Gamma_{41}$. The unperturbed population is n in m^{-3}, Γ_{41} in s^{-1} is the rotational transfer from level 4 to 1, and Γ_{14} is the rotational transfer in the opposite direction. The rotational transfer from level 1 to level 4 is assumed to be the same as between levels 2 and 3. Also, each Zeeman state in level 1 or 4 is assumed to be equally likely populated by rotational transfer collisions, and rotational transfer rates from lower laser-coupled states to their respective bath levels are assumed equal.

Neglecting the pure dephasing rate for the coherence between states a and b, the de-phasing rate γ_{ab} between states a and b is given by

$$\gamma_{ab} = \frac{1}{2}(\Gamma_a + \Gamma_b). \qquad (1)$$

We also assume that

$$\gamma_{ab} = \gamma_{as}, \qquad (2a)$$

$$\gamma_{ab} = \gamma_{jb}, \qquad (2b)$$

where s and j are all the states within levels 2 and 1, respectively.

The following additional assumptions are made: Vibrational transfer and collisional quenching occur only between levels 3 and 4, changes in the orientation of a level due to collisions without population transfer are negligible, and also velocity-changing collisions are negligible.

2. Multi-axial-mode laser model

In the multi-axial-mode laser model incorporated in the code, the distribution of mode frequencies and amplitudes, as well as phase relationship between the modes are well defined. The angular frequency spacing $\Delta\omega_M$ (s^{-1}) between two adjacent modes for a multi-axial-mode laser with a cavity length of L is given by [12]

$$\Delta\omega_M = \frac{\pi c}{L}. \qquad (3)$$

The mode detuning $\delta_{n,l}$ from line center ω_L is calculated from the equation

$$\delta_{n,l} = \Delta\omega_M \left[l - \frac{N_l + 1}{2} \right], \qquad (4)$$

where l is the mode number, and N_l is the total number of modes.

The spectral distributions of pulse-averaged mode amplitudes are described by a Gaussian profile with a full width at half maximum (FWHM) of $\Delta\omega_L$, where ω_L is the angular frequency of the laser radiation in the laboratory frame.

The actual laser parameters incorporated in the code are as follows: The laser linewidth in the input file was taken to be 0.3 cm^{-1} (cf. Sec. III). The mode spacing is calculated to be 0.034 cm^{-1} from the cavity length. This value was confirmed by measuring the mode profile with an etalon.

The phases of different modes are assumed to be random and independent. The phase for each mode can assume a random value from 0 to 2π and is assumed constant during each pulse. Modes with average amplitude of at least 1% of the average peak amplitude of the central mode are considered, and their total number is calculated from the laser bandwidth and mode spacing.

The mode amplitudes are assumed to be exponentially distributed to account for the fluctuations in the spontaneous emission noise for each of the modes in the initial phase of the laser pulse [12,21,22].

$$A_{0,l} = -\overline{A_{0,l}}\ln(1 - \xi_l), \qquad (5)$$

where $A_{0,l}$ is the amplitude of the electrical field of mode l and $\overline{A_{0,l}}$ is its time average. The random term ξ_l can assume any value between 0.001 and 0.999.

3. Multi-axial-mode DNI calculations

The direct numerical integration of the time-dependent density-matrix equation was performed using the subroutine DEABM of the Sandia Fortran Slatec library, which utilizes a fifth-order Adams-Bashforth-Moulton predictor-corrector ordinary differential equation solver [23].

The code was compiled with Microsoft developer studio with FORTRAN 90 module. It was run on a computer with a Pentium II 450 MHz processor and Windows 98. The calculation time depends greatly on the number of time steps, modes, velocity groups, and the type of broadening incorporated in the calculation and other parameters discussed below.

The Doppler effect is incorporated in the analysis by dividing the population of the state M_b into different velocity groups. Interaction with the laser is assumed not to change the velocity of the molecule, and velocity-changing collisions are also neglected.

If only homogeneous broadening is considered, the calculation time for 100 single-pulse intensities varies between 3 and 4 h. The calculation time increases to about 36–40 h (depending on the frequency separation assumed between the velocity groups) when Doppler broadening is included. Using the small-angle approximation, only the velocity components in a single direction are considered. The incorporation of Doppler broadening in the calculations is discussed in more detail in Giancola et al. [12].

Doppler and collisional widths were calculated as discussed in the Appendix. The product of the number of velocity groups and the frequency separation between velocity groups was specified to be at least twice the FWHM of the Doppler profile. The number of time steps is another input parameter, which greatly affects the running time and the convergence of the results. For multi-axial-mode laser pulses the laser intensity will vary on time scales corresponding to the inverse of the laser bandwidth due to mode beating. The fastest oscillations are due to the beating of the two modes with the greatest frequency spacing. In this case, mode 1 is at $\omega_L - 0.34$ cm^{-1} and the last mode is at $\omega_L + 0.34$ cm^{-1}. Therefore the fastest beat frequency is 0.68 cm^{-1}. In gen-

eral, the following equation is used to determine the required time steps:

$$n_{steps} = 10(2\delta_{l,l})ct_{int}, \tag{6}$$

where n_{steps} is the total number of time steps required, $\delta_{l,l}$ is the detuning frequency of the first mode (0.34 cm^{-1}), and t_{int} is the total integration time in s, which is set to 20 ns.

The computer code of Giancola *et al.* [12] was modified slightly to simulate the co-propagating geometry of our experiment (cf. Sec. III). For the co-propagating geometry the Doppler shift in frequency for a given velocity group will be the same for the pump and probe beams.

4. Calculation of saturation curves

The input parameters for the different experimental cases are the same except for the collisional width, Doppler width, number of velocity groups considered, and the frequency separation between velocity groups. The collisional width varied according to changes in pressure, temperature, and species concentration. The pressure was recorded experimentally, and the temperature and the species concentration were calculated from flame simulations (cf. Appendix). The approach used to calculate the collisional width and Doppler width was adopted from Reichardt *et al.* [24], which led to excellent agreement with experimental data in their analysis. As expected, the contribution of water vapor and carbon dioxide to the collisional width was the most significant. The Doppler width was calculated from the formula

$$\Delta\omega_D = \omega_0 \sqrt{\frac{8(\ln 2)kT}{mc^2}}, \tag{7}$$

where $\Delta\omega_D$ is the Doppler width, ω_0 is the resonance angular frequency in s^{-1}, k is the Boltzmann constant in J/K, and m is the mass of OH in kg. For the experiments in this work the Doppler width was approximately 0.25 cm^{-1}.

B. Simple model for the PS saturation process

One of the main drawbacks of the DNI code for PS is its restricted practical applicability in a given situation. In a real measurement situation one cannot derive, for example, saturation curves from the DNI code without knowing numerous parameters such as species concentration, collision rates, and so forth; and yet these may be the very parameters one seeks to determine by such measurements. A recursive application of DNI simulations is possible in theory, but as every DNI run takes an appreciable amount of time (cf. Sec. II A 3) this approach seems hardly feasible. On the other hand, the DNI approach is a very useful tool for testing various aspects of PS signals and in searching and validating simple analytical expressions that describe the PS process. Such expressions may render it feasible to extract parameters like those mentioned above from a measurement. This was already demonstrated for DFWM using a similar approach [25].

To elucidate our proposal of such a simple analytical expression we discuss first a similar expression for the signal strength in DFWM. Abrams and Lind derived such an ana-

lytical expression for stationary two-level atoms by directly solving the Liouville equation [26,27]. For weak absorption within the interaction volume of the beams, the pump-intensity dependence of the DFWM signal intensity can be written as

$$I_{DFWM} = r_{DFWM} \times I_{probe}, \tag{8a}$$

where I_{probe} is the probe pulse intensity in W m^{-2} and r_{DFWM} the DFWM reflectivity [28]. The latter is given as

$$r_{DFWM} = a\frac{(I_{pump}/I_{sat}^{DFWM})^2}{(1+4I_{pump}/I_{sat}^{DFWM})^3}n^2, \tag{8b}$$

where a is a scaling factor, I_{pump} is the pump-pulse intensity, I_{sat}^{DFWM} the DFWM saturation intensity, and n the number density of the optically pumped constituent. The DFWM saturation intensity for a monochromatic excitation source equals [26,27]

$$I_{sat}^{DFWM} = \frac{\pi\hbar^2\epsilon_0 c\Gamma\Delta\nu_c}{|\mu|^2}, \tag{9}$$

where $\hbar$ is the Planck constant divided by 2π in J s, Γ is the depopulation rate of the excited level, $\Delta\nu_c$ is the collisional linewidth in s^{-1}, and μ is the dipole moment—in mA s—of the excited transition. For an atom or a molecule with degenerate Zeeman sublevels coupled by the laser light one would not expect that Eq. (8) holds since the pump rate of all sublevels depends on their respective magnetic quantum numbers m_J, which leads to m_J-dependent saturation intensities for different Zeeman sublevels. These m_J-dependent saturation intensities would enter Eq. (8b). Reichardt and Lucht [25] showed in contradiction to the reasoning above, that transitions in OH $A\,^2\Sigma^+ - X\,^2\Pi(0,0)$ and in CH $X\,^2\Pi - A\,^2\Delta$ are well described by Eq. (8). Therefore one could be led to assume that PS-saturation curves may also be described by a single saturation intensity. This assumption is supported by the findings of Suvernev *et al.* [20], who pointed out that the theory of PS can mathematically be treated as a special case of DFWM for which the two DFWM pump beams are co-propagating. Another indication are the findings of Ritze *et al.* [29]. They solved the stationary Liouville equation for all magnetic sublevels and showed that the PS-signal strength can be written as a function of a single saturation intensity. In their model they assume plane waves, and also that phase and population relaxation rates equal each other. The effect of Doppler broadening is also incorporated into their theory. Nonetheless, their approach is limited to single-mode lasers only and puts certain restraints on the relaxation rates. Their approach does not result in a simple algebraic solution but results in a sum of functions that has to be evaluated numerically. Following these findings we seek an expression for the PS reflectivity similar to Eq. (8b). According to this equation, the DFWM reflectivity has a maximum for $I_{sat}^{DFWM}/2$ and decreases for higher pump intensities. PS reflectivities have been measured by many authors [5,9,12,19,30], but a decrease of the PS reflectivity for high pump intensities has not been observed. Therefore
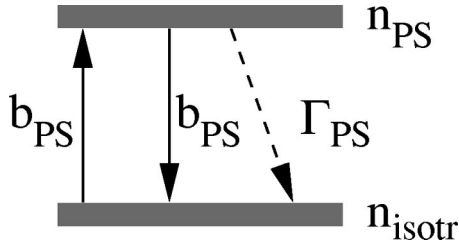
FIG. 1. Stationary two-level system for a simple model of the PS pumping process. n_{isotr}, number density of isotropically oriented molecules; n_{PS}, number density of aligned molecules; b_{PS}, pump rate from one level to the other; Γ_{PS}, transition rate due to the combined effect of spontaneous emission and collisions.

one cannot use Eq. (8b) in a straight forward fashion to describe PS-saturation curves. Measurements by Nyholm *et al.* [5,30] indicated that the PS reflectivity depends on $(I_{pump})^2$ for nonsaturated regimes. Suvernev *et al.* [19], Reichardt and Lucht [11], and Giancola *et al.* [12] showed that the PS reflectivity becomes nearly independent of I_{pump} in saturated regimes, i.e., $r_{PS} \propto (I_{pump})^0$. Similar to Eq. (8) we propose hence the following simple analytical expression for the PS signal intensity I_{PS}:

$$I_{PS} = r_{PS} I_{probe} \tag{10a}$$

with

$$r_{PS} = a \left(\frac{n}{1 + I_{sat}^{PS}/I_{pump}} \right)^2, \tag{10b}$$

where I_{sat}^{PS} is the so-called PS saturation intensity. The proposed PS reflectivity satisfies the aforementioned dependence on the pump intensity. Equation (10) can be described by the following simple two-level model (see Fig. 1). The PS signal is generated by coherent forward scattering of the probe beam [31]. The scattering medium consists in this case of aligned molecules (n_{PS}, see Fig. 1), i.e., $r_{PS} \propto (n_{PS})^2$. These molecules are generated by the polarization-dependent pumping ($b_{PS} = B_{PS} I_{pump} C_{al}/c$ in s^{-1}, where B_{PS} is proportional to the Einstein B coefficient in $m^3 s^{-2} J^{-1}$ and C_{al} in s is the overlap integral of laser and absorption line) of isotropically distributed molecules (n_{isotr}). The pumped level can be depopulated by stimulated emission (b_{PS}), by collisions, or by spontaneous emission (Γ_{PS}). The dependence of n_{PS} on the pump intensity is given as (see, e.g., [4], Chap. 7.2.1)

$$n_{PS} = \frac{1}{1 + I_{sat}^{PS}/I_{pump}} \frac{n}{2}, \tag{11a}$$

where

$$I_{sat}^{PS} = \frac{c \Gamma_{PS}}{2 B_{PS} C_{al}}. \tag{11b}$$

Notice that these equations only hold for homogeneously broadened absorption lines, viz., stationary absorbers. Recalling that $r_{PS} \propto (n_{PS})^2$ one obtains Eq. (10b) from Eq. (11a).
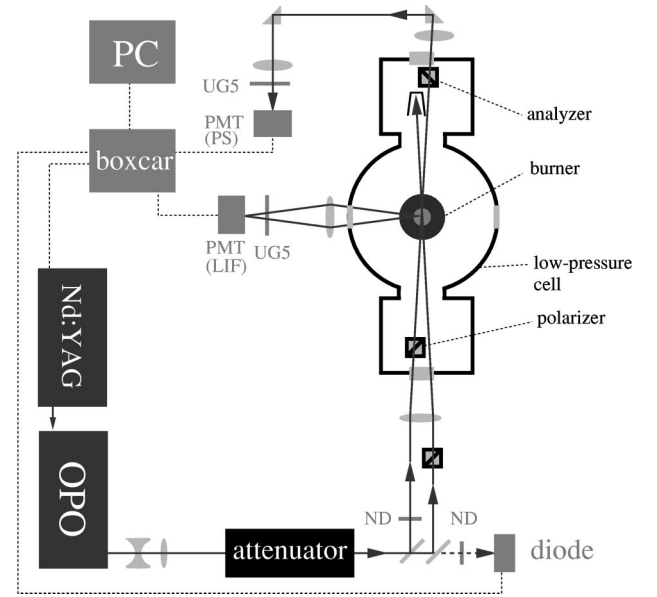

FIG. 2. Experimental setup. Apertures and pinholes are omitted for clarity. ND, neutral density filter; PMT, photomultiplier; UG5, Schott color filter.

The generation of anisotropically oriented molecules is caused by the Zeeman-level dependence of the optical pumping rate. The polarization-dependent pumping strength (B_{PS}) can thus be described as a function of the difference in pumping strength for different Zeeman levels.

To validate the model presented here the generic function for the PS signal intensity [Eq. (10)] was fitted to measured and calculated saturation curves (see Sec. IV).

III. EXPERIMENTAL SETUP

The probed molecule in our experiments was the OH radical, which frequently occurs in combustion processes, where it is one of the most important oxidizers [32]. Its spectroscopic characteristics are ideal for these experiments since it is easily excited in UV light using common laser sources and has a well-understood spectrum [33–35]. The absorption lines of OH are, in contrast to other common diatomic molecules in combustion processes, well separated even at well-elevated temperatures and pressures. A sketch of the experimental setup is found in Fig. 2.

An optical parametrical oscillator (OPO, Spectra Physics, MOPO 730-10) served as the excitation light source. The OPO was pumped by a single (longitudinal) mode Nd:YAG laser (Spectra Physics, PRO 290-10). The laser's pump energy was 550 mJ/pulse at 355 nm (third harmonic) with a pulse duration of 5–6 ns. The OPO was operated at 619 nm (signal) and the output of the OPO was frequency doubled in a BBO crystal to yield a typical pulse energy of around 6 mJ at 309 nm. The linewidth in the visible is specified by the supplier to $\Delta \nu_{laser} = 0.2$ cm^{-1}, the pulse duration to $\Delta t = 3-4$ ns.

To enlarge the diameter of the outcoming ultraviolet laser beam, a Galilean telescope ($f = -40$ mm and $+150$ mm) was used. After this the central part of the beam profile was

selected with an aperture and the profile was then spatially filtered by two consecutive apertures of approximately 6 mm diameter placed at a distance of 1 m. The energy of the filtered beam could be continously varied over one order of magnitude by a beam attenuator (Newport, 935-10). After passing the attenuator the beam went through a 45° quartz-plate beam splitter. The reflected beam was attenuated by neutral-density filters and served as the probe beam. The transmitted beam was used as the pump. A surface reflection was used to monitor the laser pulse energy with a fast photodiode on a shot-to-shot basis (Elliot, DET200). After the turning prism the remaining part of the pulse served as the pump pulse and passed a Glan-type polarizer (B. Halle Nachfl., PGL 10), which polarized the beam at 45° from the horizontal. Typical pump energies after the polarizer ranged up to 250 μJ. The probe beam energy was $\beta = 0.5\%$ of the pump energy. The extinction of the polarizers used in the experiment were specified to be better than 10^{-5}.

The probe and the pump beams passed through a 500-mm focusing lens and entered the cell of a low-pressure burner in the co-propagating beam geometry . The burner is described in detail below after this general description of the overall measurement setup. In the cell the probe beam passed through another polarizer, which polarized the probe beam horizontally to prevent depolarization by window birefringence. The beams were crossed in a copropagating beam geometry at an angle of 4.9° centered above a McKenna-type burner head. The focal sizes of probe beam, $d_{probe} = 354 \pm 24$ μm, and pump beam, $d_{pump} = 402 \pm 23$ μm, were measured by translating a knife edge across the beams. The pump beam was blocked inside the cell. The probe beam propagated through the analyzer. The probe beam was spatially filtered and imaged through a 200-μm pinhole onto a photomultiplier (PMT, Hamamatsu R758, No. EB0382) situated 1.5 m from the beam crossing point. In this way flame background emission and LIF signals were effectively eliminated from the signal channel.

To facilitate the alignment of the PS system, LIF from the crossing point was collected at 90° angle through a window using a 100-mm lens and imaging through a pinhole onto another PMT (same model as above). To suppress laboratory and other background light, absorption filters (Schott, UG5) were mounted directly in front of the the entrance pinholes to both PMTs.

Signals from photodiodes and PMTs were preamplified (SR245) and passed through gated integrators (SR250) from Stanford Research Systems before storage on a PC.

The low-pressure burner facility was specially designed for the present PS experiments to include the polarizers and thus to avoid problems associated with window birefringence at different operating pressures. Polarizer and analyzer were contained in specially designed sections on the sides of the main chamber. They were mounted in special rotation stages and the crossing angle at the analyzer could be adjusted by a pressure-sealed shaft from the outside of the cell. A sketch of the burner is found in Fig. 3. It consisted of three main parts: the main cell, the burner head on a translation stage, and the two sidearms containing the polarizers. The burner head was of plug type with a plug diameter of 30 mm. Fuel (methane)
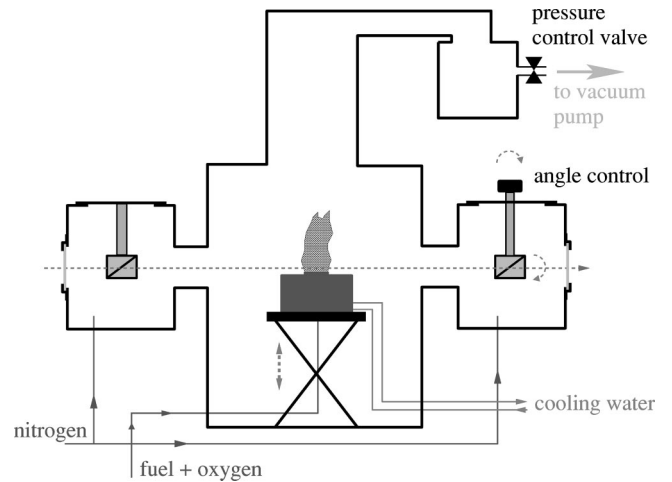

FIG. 3. Side view of the low-pressure burner. Beam path of pump beam not shown.

and oxygen were mixed and regulated by two mass-flow controllers (Bronkhorst, El-Flow). The burner head was water cooled and mounted on a vertical translation stage, driven by a stepper motor with 1 μm resolution. Exhaust gases were extracted through a water-cooled upper section by a rotary-vane vacuum pump (Leybold, Trivac 16B) with a maximum pump speed of 16.5 m^3/h.

To keep the polarizers free from water condensation and also to allow fine adjustment of the gas pressure, the gas cell could be flushed with dry nitrogen at flows up to 15 standard l/min. The gas pressure could be continously regulated from 20 mbar up to atmospheric pressure by adjusting both pump speed and nitrogen flow. The pressure was measured with a capacitance manometer (CCM Instruments).

Flame conditions were stoichiometric for all experiments presented here, with flows of 0.25 standard l/min for methane and 0.5 standard l/min for oxygen.

The photodiode signals were calibrated on an absolute scale against readings from an energy meter (Laser Probe, RjP-636 and Rm-3700). The quote of the pump energy in the crossing point to the measured energies above was measured once with a calibrated photo-diode (Ophir, AN/2 and PD-330-UV) and this quote was then used to obtain the pump energy in the crossing point for all measurements.

OH was excited at 309.683 nm on the $Q_2(8)$ 8 line in the $A\,^2\Sigma^+ - X\,^2\Pi(0,0)$ branch. The line absorption strength of the chosen line depends only weakly on temperature (see [4], Chap. 7.2.4).

IV. RESULTS AND DISCUSSION

A. Homogenous line broadening

Due to the elevated temperature in the low-pressure flame, the Doppler linewidth in the probe volume was approximately 0.25 cm^{-1}, which is substantially larger than the collisional linewidth (<0.07 cm^{-1}, see Table I). Therefore, one needs to excite the OH molecule with a laser field exhibiting a bandwidth smaller than the homogenous linewidth in order to attain saturation curves that are dominated
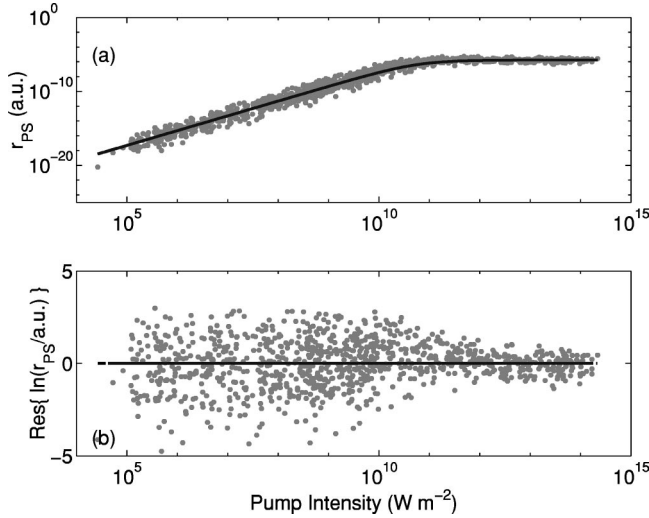
FIG. 4. (a) Result of a DNI simulation for the copropagating beam geometry and a homogenous linewidth of 0.08 cm^{-1}. The pumped transition is $Q_2(8)$ 8 A $^2\Sigma^+ - X$ $^2\Pi(0,0)$ of OH. The fit of the saturation model [Eq. (10)] (solid line) to the logarithm of the PS reflectivities yields a PS saturation intensity of 5.9 $\times 10^{10}$ W m^{-2}. (b) Residuals of the fit.

by homogenous line broadening. A laser system featuring so small a bandwidth was not available, which is why only results from DNI calculations are available for the case of homogenous line broadening.

DNI calculations were conducted for the laser parameters specified in Secs. III and II A and several collisional widths (0.08–0.4 cm^{-1}). An example for $\Delta\nu_c = 0.08$ cm^{-1} is shown in Fig. 4(a). The chosen pump intensities cover both the unsaturated and the saturated regime, spanning over ten orders of magnitude. The fit of Eq. (10b) to the logarithm of the PS reflectivity yields an excellent agreement, as can be seen from the residuals in Fig. 4(b). The P value[1] of this particular fit is 37%. Due to the exponentially distributed intensity of the axial-laser modes (cf. Sec. II A 2) the distribution of the calculated PS reflectivities is non-normal, whereas the logarithmic values follow an approximately normal distribution. This is why weighted least-squares fitting, which relies on normal distributed samples, was applied to the logarithm of the PS reflectivities.

An interesting objective is to determine how the fit parameters a and I_{sat}^{PS} in Eq. (10b) depend on the collisional width. For a monochromatic laser the overlap integral in Eq. (11b) is a Lorentzian function, i.e.,

$$C_{al} = C_{Lorentz} = \frac{\Delta\nu_c}{4\pi^2(\nu_{laser} - \nu_{line})^2 + (\Delta\nu_c/2)^2}, \quad (12)$$

_____

[1] The P value determines the probability to obtain a fit with a worse goodness than the actual one, i.e., low P values indicate unlikely fits. For data sets with many data points, as is the case here, the P values of unbiased fits are centered around 50%. For a discussion of the P value and a comparison of significance, see [36], Chap. 2-4.1.

where ν_{laser} is the laser frequency in s^{-1} and ν_{line} is the line-center absorption frequency. For maximum overlap, i.e., $\nu_{laser} = \nu_{line}$, this equation yields $C_{Lorentz} = 4/\Delta\nu_c$. Inserting the latter into Eq. (11b) yields

$$I_{sat}^{PS} = \frac{2c\Gamma_{PS}\Delta\nu_c}{B_{PS}} \propto \frac{12\hbar^2\epsilon_0 c\Gamma_{PS}\Delta\nu_c}{|\mu|^2}, \quad (13)$$

where the relation $B_{PS} \propto B = |\mu|^2/6\pi^2\epsilon_0\hbar^2$ was used. Assuming that Γ_{PS} equals the depopulation rate, the expression for the PS-saturation shown in Eq. (13) agrees well with that for the DFWM saturation intensity [cf Eq. (9)]. For the DNI calculations $\Gamma = R_c \propto \Delta\nu_c$ (see Sec. II A 1 and the Appendix) and one expects according to Eq. (13) that the PS-saturation intensity depends on the square of the collisional width.

The scaling factor in Eq. (10b) is a measure of the scattering efficiency of the probe photons at the anisotropically distributed molecules. As a first assumption one may propose that this efficiency is proportional to the overlap of the laser and absorption-line profiles, i.e., C_{al}. For a monochromatic laser and maximum absorption one expects hence

$$a \propto C_{Lorentz} = \frac{4}{\Delta\nu_c}. \quad (14)$$

To investigate the dependence of the fitting parameters on the collisional width, the following equations were fitted to the former:

$$a = d_1(\Delta\nu_c)^{-d_2} + d_3 \quad (15a)$$

and

$$I_{sat}^{PS} = d_4(\Delta\nu_c)^{d_5} + d_6. \quad (15b)$$

The fits resulted in

$$d_2 = 1.2, \quad d_3 \ll d_1 \quad (16a)$$

and

$$d_5 = 1.7, \quad d_6 \ll d_4. \quad (16b)$$

The deviation of the exponents d_2 and d_5 from the predicted values, i.e., $d_2 = 1$ and $d_5 = 2$, is due to the finite laser bandwidth. To prove this, the same DNI calculations were conducted for a laser linewidth of 0.1 cm^{-1} and a mode spacing of 0.025 cm^{-1}. The collisional width spanned from 0.05 to 0.8 cm^{-1}. Fitting Eqs. (15a) and (15b) to the yielded parameters a and I_{sat}^{PS} resulted in this case in $d_2 = 1.0$ and $d_5 = 2.0$, i.e., an excellent agreement with the previously presented predictions.

Our generic model results in excellent fits to DNI calculations and also the dependence of the fit parameters on the collisional width is readily explained. Another check of our generic model is the PS line profile that can be derived from Eqs. (10b) and (11b). For a monochromatic laser these equations yield

$$r_{PS} \propto (C_{Lorentz})^3 \quad \text{for} \quad I_{pump} \ll \max(I_{sat}^{PS}) \quad (17a)$$
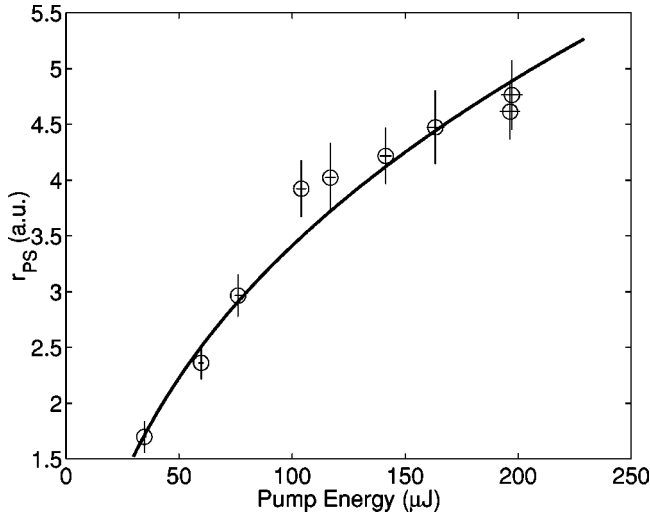
FIG. 5. Power-dependence scan for $p = 300$ mbar. Circles, means from 30 single shots; error bars, 95% confidence intervals of the mean values; solid line, fit of the empirical saturation model [Eq. (21)] to the measurement data. Estimated $E_{sat}^{PS} = 9.0$ μJ ($\triangleq 2.1 \times 10^{10}$ W m^{-2}), $e = 1.57$ (see Sec. IV B 3).

FIG. 6. Theoretical power-dependence scan for $p = 300$ mbar resulting from DNI calculations: (a) Dots, results from single DNI runs; solid line, fit of the empirical saturation model [Eq. (21)] to the logarithm of the PS reflectivities. Estimated $I_{sat}^{PS} = 2.9 \times 10^{10}$ W m^{-2}, $e = 1.57$ (see Sec. IV B 3). (b) Residuals for the PS reflectivity.

and

$$r_{PS} \propto (C_{Lorentz})^1 \quad \text{for } I_{pump} \gg \max(I_{sat}^{PS}). \quad (17b)$$

These predictions of the PS line profiles are in excellent agreement with theoretical investigations of Reichardt and Lucht [11] and with experimental investigations of New [37].

After this successful validation of our simple model of the PS signal generation we proceed to the case of inhomogenously broadened lines.

B. Inhomogenous line broadening

1. Strong saturation

An experimental power dependence scan for a pressure of 300 mbar is shown in Fig. 5. Energy values stated here are the pump-pulse energies of the interaction volume in absence of a flame. As one can see the PS reflectivity does not level out for large pump intensities, which contradicts the findings in the previous section. Our experimental findings agree on the other hand with those of Suvernev et al. [19]. They reported power-dependence scans for OH and NH, also in the co-propagating beam geometry. For NH, the measured PS reflectivities increase clearly even for pump intensities substantially larger than the saturation intensity, but the slope is smaller than for pump intensities in the unsaturated and the partially saturated regime.

Our experimental findings were compared with DNI calculations. The theoretical power-dependence scans were found to feature a similar slow increase of the PS reflectivity for very large pump intensities [see Fig. 6(a)]. The fits shown in Figs. 5 and 6 are discussed later on (Sec. IV B 3). We explain the different saturation behavior in the case of inhomogenous line broadening as follows. Various velocity classes of the probed molecule are excited as the laser and the Doppler linewidth are larger than the collisional line-
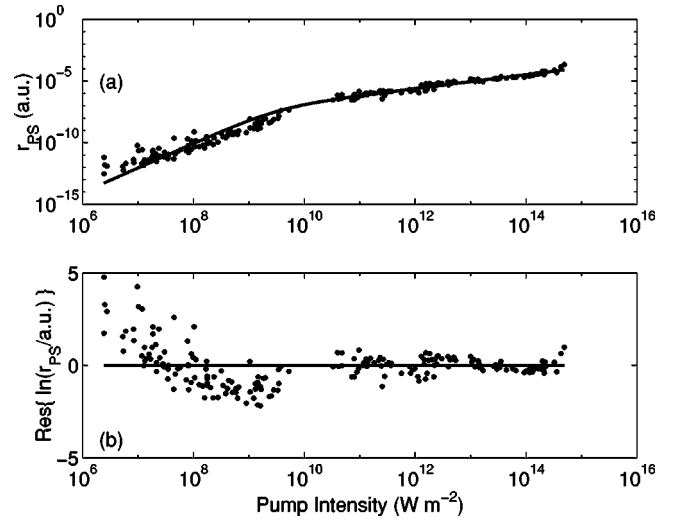
width. The center part of the absorption-line profile will saturate first for a laser frequency tuned on the absorption maximum. As the pump intensity approaches the saturated regime the wings of the profile, which belong to other velocity classes and which are pumped at lower rates, are still unsaturated and entail a not fully saturated PS reflectivity. This is not the case for homogenous line broadening, for which the whole line profile is saturated at the same pump intensity.

With these findings we can provide an explanation for the disagreement between our simple analytical model and the curves in Figs. 5 and 6. The observed deviation originates from the fact that our simple model does not account for inhomogeneous line broadening of the absorption line, which may arise in the case of dominating laser and Doppler line width. If the dominating line broadening is mainly homogenous and/or the molecule is probed in a Doppler-free geometry with a narrow-bandwidth laser, no saturation broadening occurs and our analytical model gives an excellent description of the PS-saturation behavior as discussed in the previous section.

2. Partial saturation

Since the Doppler linewidth in our experiment was not much smaller than the laser bandwidth one could expect that our generic model provides an adequate prediction of power-dependence scans in the partially saturated regime. In this section we investigate power-dependence scans for which the highest pump intensities are of the same order of magnitude as the PS-saturation intensities. PS-saturation curves were measured for different gas pressures. For each measurement the pressure was held fixed at a constant value and the PS signal recorded for different settings of the laser pulse energy.

An example of such a scan for $p = 700$ mbar is shown in Fig. 7(a). Each measurement point consists of 150 single
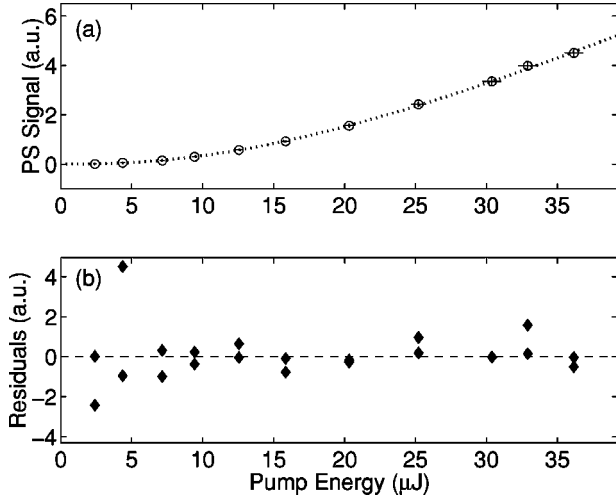
FIG. 7. Power-dependence scan for $p = 700$ mbar: (a) The circles stand for the mean values, the error bars for the 95% confidence intervals of the mean values (150 single shots). Dotted line, saturation model [Eq. (18)] fit to the data, estimated $E_{\text{sat}}^{\text{PS}} = 20$ μJ ($\triangleq 4.8 \times 10^{10}$ W m^{-2}); $P = 40\%$. (b) Residuals of the fit.

shots. Equation (10) was fitted to each saturation curve. In this particular experiment, pump and probe intensity were varied simultaneously ($I_{\text{probe}} = \beta \times I_{\text{pump}}$, see Sec. III), consequently Eq. (10) had to be slightly modified and was modified to comprise the measured pump energies instead,

$$I_{\text{PS}} = a\beta \frac{(E_{\text{pump}})^3}{(E_{\text{pump}} + E_{\text{sat}}^{\text{PS}})^2} + b, \qquad (18)$$

where a, $E_{\text{sat}}^{\text{PS}}$, b, and the pump energies were the parameters to be estimated. The offset b was introduced to account for the statistical uncertainty of the subtracted background.

In nonlinear signal generation pulse-to-pulse fluctuations of the laser intensity lead to skewed signal distributions, which in their turn result in biased estimates for model parameters if conventional least-squares fitting approaches are used. Therefore, we developed a generalized fitting scheme that yields unbiased estimates from such data. This method is discussed in detail in a forthcoming paper [38] and was used for the parameter estimation in this work.

When using Eq. (18) for fitting, one tacitly assumes that the absorption of both probe and pump beam over the flame diameter is weak. Absorption measurements revealed, for the same pressure range as in our work, peak absorption up to 37% when passing the flame on the center line [16]. The approach presented below was used to account for the absorption and was found to lower the estimated PS-saturation intensities by up to 10%.

Known values of I_{probe} and I_{pump} in the interaction volume in the absence of a flame are taken as the initial values for the beams entering the flame. It is assumed that the diameter of the pump and probe beams do not change over the flame diameter, which is a reasonable assumption as the diameter of the flame (30 mm) is of the same size as the Rayleigh range (40 mm). The transmission of a beam from outside the flame to the interaction volume can be calculated by solving the following equation (cf. [39], Chap. 8.6.3):

$$\ln \frac{T}{T^*} = (1 - T) \frac{I}{I_{\text{sat}}^{\text{abs}}}, \qquad (19)$$

where T^* is the measured transmission for a nonsaturating beam, T is the transmission for the actual intensity I, and $I_{\text{sat}}^{\text{abs}}$ is the absorption saturation intensity. The intensities I were calculated from the measured energies with aid of Eq. (20) (see below). In the Appendix it is explained how the saturation intensity was obtained. The values of $I_{\text{sat}}^{\text{abs}}$ listed in Table I were assumed to be valid over the whole radial extent of the flame.

Figure 8 shows the calculated transmission corresponding to the PS-saturation curve in Fig. 7(a). The probe beam transmission depends only weakly on its intensity as the latter is substantially smaller than the saturation intensity. The pump beam transmission varies strongly for small intensities and levels out to a value close to unity for elevated intensities.

The impact of the calculated transmission of probe and pump beam was introduced into Eq. (18) by replacing the unperturbed energies with their transmitted values, i.e., $E_{\text{probe}} \rightarrow T_{\text{probe}} E_{\text{probe}} = \beta T_{\text{probe}} E_{\text{pump}}$, and $E_{\text{pump}} \rightarrow T_{\text{pump}} E_{\text{pump}}$, respectively. This corrected form of Eq. (18) was fitted to the same saturation curves as for Fig. 9 below and the estimated PS-saturation intensities were found to be 5–10 % lower than the corresponding values for neglected absorption. The fits with absorption-corrected probe and pump intensities did not result in noticeably better fits than without absorption correction. This surprisingly small differ-

TABLE I. Parameters for the interaction volume. The values served as input data for the DNI calculations. p, pressure for the measurement; columns 2–4, the mole fractions of OH, CO$_2$, and H$_2$O; T, temperature; Q, quenching rate; $\Delta\nu_c$, collisional width; $I_{\text{sat}}^{\text{abs}}$, absorption saturation intensity. For a discussion, see the Appendix.

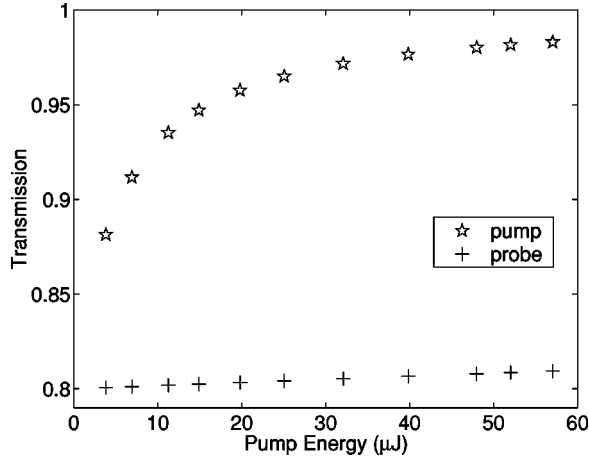| p (mbar)	x_{OH}	x_{CO2}	$x_{\text{H}_2\text{O}}$	T (K)	Q (s^{-1})	$\Delta\nu_c$ (cm^{-1})	$I_{\text{abs}}^{\text{sat}}$ (W m^{-2})
30	2.2×10^{-2}	0.22	0.52	1920	3.6×10^7	1.9×10^{-3}	2.4×10^8
100	7.8×10^{-3}	0.30	0.62	1700	1.7×10^8	8.1×10^{-3}	1.1×10^9
300	8.3×10^{-3}	0.30	0.63	1880	4.3×10^8	2.3×10^{-2}	2.9×10^9
500	5.8×10^{-3}	0.31	0.64	1860	7.4×10^8	3.8×10^{-2}	4.9×10^9
700	4.5×10^{-3}	0.31	0.65	1840	1.1×10^9	5.3×10^{-2}	7.1×10^9
900	3.7×10^{-3}	0.32	0.65	1830	1.4×10^9	6.9×10^{-2}	9.2×10^9

FIG. 8. Calculated transmission for probe and pump beam to the crossing point of both (center line of the flame). Same experimental conditions as for Fig. 7.

ence for the PS-saturation intensities is explained as follows. The chosen pump intensities were so high, that T_{pump} was close to unity for most of the energy settings (cf. Fig. 8). Therefore, the impact of absorption on $T_{pump}E_{pump}+E_{sat}^{PS}$ in the denominator of Eq. (18) is small and the absorption affects mainly the scaling factor a. The results presented below were estimated assuming zero absorption, i.e., with the uncorrected form of Eq. (18).

In Fig. 7(b) the residuals of the fit are shown. They exhibit a near-stochastic distribution and the fit was characterized by a high P value ($P=40\%$). From both findings it can be concluded that our proposed analytical model containing a single PS-saturation intensity fits very well to the measured saturation curve within the error margins. None of the fits to the experimental PS-saturation curves showed P values higher than 50%, although the residuals were almost normal distributed. From this observation one concludes that the estimated variances and covariances of signal intensity and pump energy are somewhat too small. A possible explanation
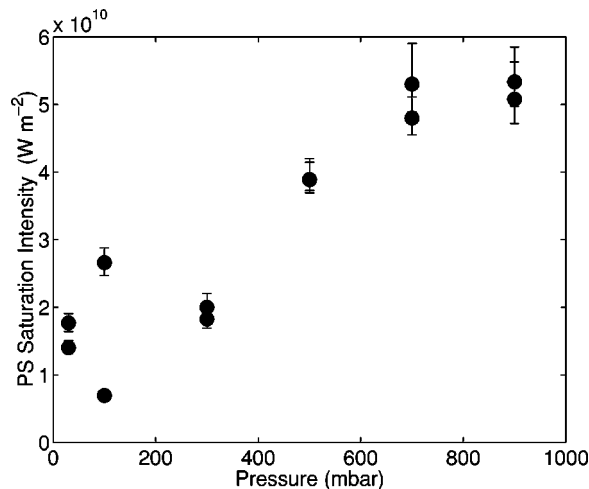

FIG. 9. Experimental PS saturation intensities for different pressures. The symbol for $p=500$ mbar consists of two measurement points with nearly equal saturation intensities.

for this is an additional variation of the PS signal from one energy setting to the other, which is not reflected by the statistical variation of the measurement points within one energy setting. The pulse energy was varied by tuning two mirrors within a beam attenuator (cf. Fig. 2). We suppose that this imposed a mechanical stress on the optical table, which resulted in a small nonsystematic change of the alignment and consequently of the signal strength between two consecutive energy settings. This could explain why Eq. (18) yields almost unbiased fits but with too low P values.

Confidence intervals of the estimated parameters for each saturation curve were obtained by running 1000 Monte Carlo simulations for each power-dependence scan (see [40], Chap. 14.5). As we did not have any measure for the proposed nonsystematic change of the alignment, only the statistical uncertainties of the measured values were used for the Monte Carlo simulations. This leads to consequently somewhat too small confidence intervals for the estimated parameters. All errors quoted in the following stand for 95% confidence intervals estimated by this approach.

The results of the fits of Eq. (18) to all measurements are shown in Fig. 9. The estimated PS-saturation energies were transformed into intensities with the relation

$$I=\frac{4E}{\pi(d_{pump})^2\Delta t},\qquad(20)$$

using the values quoted in Sec. III. The uncertainties of the factors in Eq. (20) were quadratically added to the uncertainty of I_{sat}^{PS} from the Monte Carlo simulations.

The PS saturation intensity in Fig. 9 is observed to increase with the gas pressure, which means that the destruction of the anisotropy induced by the pump beam takes place at a higher rate Γ_{PS} at higher pressures. This agrees with our findings in Sec. IV A.

The reproducibility of the estimated PS-saturation intensities is good for $p\geq300$ mbar and minor below. The observation discussed above, namely that the shown confidence intervals are too small, could explain the nonoverlapping error bars, especially for $p=30$ mbar. Another possible error source is the stability of the probed flame. The feeding gas velocity at the burner plate in our experiment depended inversely on the gas pressure; the flame expanded from some millimeters height at elevated pressure to several centimeters for pressures below 300 mbar. Therefore small fluctuations of the pump speed may have a pronounced impact on the flame size and geometry at lower pressures. When the flame structure at the interaction section varies, this may have a substantial influence on the local collision rate and absorption and hence on I_{sat}^{PS} too.

DNI simulations were conducted for the same range of pump intensities and the same flame conditions as for the experiments (cf. Table I), and subsequently the calculated power dependence scans were analyzed by fitting Eq. (10b) to the logarithm of the PS reflectivities. This was done with weighted least-squares fitting as for the fits reported in Sec. IV A. An example for $p=700$ mbar is shown in Fig. 10(a). The fits resulted in excellent P values for pressures over 500
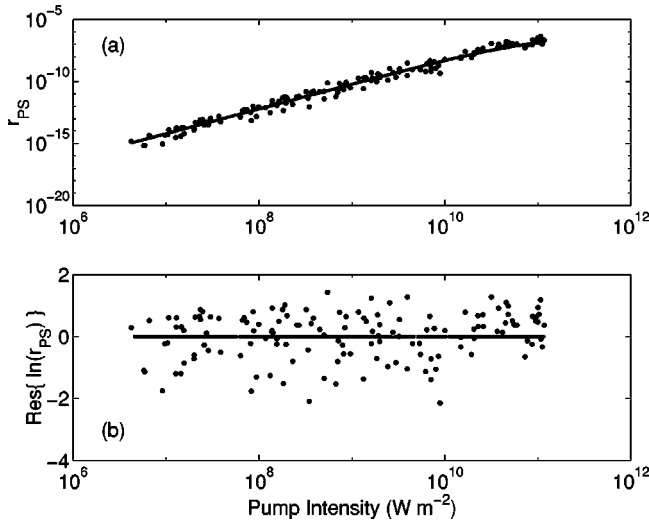
FIG. 10. Theoretical power-dependence scan resulting from DNI calculations for $p = 700$ mbar. (a) Dots, result of single DNI runs; solid line, fit of the saturation model [Eq. (10b)] to the logarithm of the PS reflectivities, estimated $I_{sat}^{PS} = 8.6 \times 10^{10}$ W m^{-2}; $P = 49\%$. (b) Residuals for the PS reflectivity.
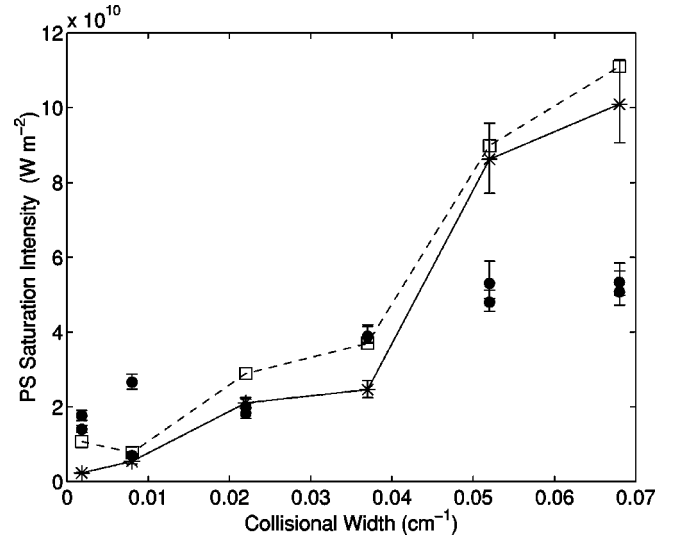

FIG. 11. Comparison of theoretical (stars/solid line, squares/dashed line) and experimental PS saturation intensities (circles) as a function of the collisional width. Stars, fit of the saturation model [Eq. (10b)] to DNI calculations for the partially saturated regime (see Sec. IV B 2); squares, fit of the empirical saturation equation (21) to DNI calculations stretching from the unsaturated to the strongly saturated regime (see Sec. IV B 3).

mbar ($P \sim 50\%$) and poor P values below that pressure ($P < 2 \times 10^{-3}$). The reason for the latter is that the DNI calculation lies systematically above the fit curve for low pump intensities ($I_{pump} < 10^9$ W m^{-2}). This feature is not observed for the experimental data, which is due to detector noise and due to that most of the conducted power-dependence scans did not cover so low an intensity. The systematic deviation of fit function and DNI calculations is due to the previously discussed feature of saturation curves for inhomogeneously broadened absorption lines, i.e., a nonvanishing increase of the PS signal in the strongly saturated regime. For the lower-pressure values the PS-saturation intensity is roughly four times smaller than the maximum pump intensity and the saturation curves exhibit clear signs of inhomogenous line broadening.

Estimated PS-saturation intensities from the DNI simulations and the experiment are shown as a function of the calculated collisional width (cf. Table I) in Fig. 11. The agreement between experiment and theory is bad for collisional widths below 0.005 cm^{-1}. At the corresponding pressure the probed flame was not formed as a horizontal disk in close proximity to the burner head, as it was the case for higher pressures, but extended some centimeters above the burner head in a cupolalike geometry. The kinetic code used for calculating the flame chemistry does not describe flames of such a geometry properly, which results in erroneous values for number densities and so forth in Table I for this particular pressure. As these values serve as input data to the DNI code the power-dependence curve calculated by the latter will not compare well to experiment. Within the "cupola" the feed gas is not fully burnt, which results in a lower temperature in this region. This entails *in praxis* higher collisional rates than in the flame simulation. The DNI calculation yields consequently lower saturation intensities. The theoretical and experimental results deviate substantially from each other for

higher collisional widths. Even this deviation may be caused by erroneous flame calculations. For these pressures the reaction zone of the flame is in close proximity to the burner head (~ 1 mm). The diffusion of flame radicals to the burner surface is consequently substantial. The reaction of flame radicals at the burner surface are modeled under the assumption of total recombination into stable constituents. This rigorous assumption may render the calculated CO_2 and H_2O concentrations in the probe volume — slightly above the reaction zone — too high, which would result in too high collisional widths and consequently too high PS-saturation intensities. Nonetheless, considering all the uncertainties in the calculations of the flame chemistry and also of the used collisional cross sections (cf. Appendix) the DNI calculations yield a very good agreement with experiment. A recently reported comparison of experiment and DNI calculations [12] showed a difference between both of the order of as much as two magnitudes, which is a noticeably stronger disagreement from the one stated here.

The proposed generic model yields in conclusion, excellent fits to experimental PS-saturation curves covering the unsaturated and the partially saturated regime. The quality of fits to DNI calculations is of poorer quality but with respect to the uncertainty of the input data for the DNI calculations both experimental and the theoretical saturation intensities agree very well.

3. Revised model for strong saturation

We will discuss two approaches to extend the presented generic model for inhomogeneously broadened lines.

The first approach is to rewrite Eq. (10b) slightly in order to provide an empirical description of the saturation curve shape,

$$r_{\mathrm{PS}} \sim \frac{(I_{\mathrm{pump}}/\tilde{I}_{\mathrm{sat}}^{\mathrm{PS}})^2}{(1 + I_{\mathrm{pump}}/\tilde{I}_{\mathrm{sat}}^{\mathrm{PS}})^e}. \qquad (21)$$

This equation features an additional fit parameter e. For $e = 2$ this equation and Eq. (10b) are identical. The former was fit to the logarithms of the data shown in Figs. 5 and 6(a). This was done with least-squares fitting. For the DNI calculations the fit reveals a bias for pump intensities below 10^{10} W m^{-2} [see Fig. 6(b)], but all the fits result in a reasonable PS-saturation intensity, both when compared to each other and also when compared to the DNI calculations for the partially saturated regime. The fit of Eq. (21) to the experimental data in Fig. 5 results in a PS-saturation intensity of 2.1×10^{10} W m^{-2} and the fit to the DNI calculations in Fig. 6 in 2.9×10^{10} W m^{-2}. The additional parameter e was 1.57 for both fits. The corresponding saturation intensity for the partially saturated regime is 2.1×10^{10} W m^{-2}. Saturation intensities from fits of Eq. (21) to DNI calculations covering both the unsaturated and the strongly saturated regime and the same parameters as for the calculations in the previous section are shown in Fig. 11 and compared to the fits to DNI calculations in the previous section. According to these results the empirical formula presented here provides a good description of PS signals in the strongly saturated regime.

Anyhow, the proposed modification of Eq. (10b) is somewhat arbitrary and it is not based on sound physical reasoning. A way to circumvent this drawback is to include the effect of inhomogenous line broadening in the stationary two-level model presented in Sec. II B. A similar task has been carried out for saturated LIF experiments with inhomogenous line broadening [41] and it would be a promising approach to modify the latter in order to even describe the observed effects in PS saturation with a simple generic model.

V. SUMMARY AND OUTLOOK

We report on the saturation behavior of polarization-spectroscopy signals. Measured saturation curves of OH for several subatmospheric pressures were compared with similar curves obtained from a detailed polarization-spectroscopy model, which comprises a direct numerical integration of the quantum-mechanical Liouville equation [11,12]. We also present a simple analytical model that was fitted to both experimental and theoretical saturation curves. Our analytical model provides an excellent description of polarization-spectroscopy-saturation curves for absorption lines dominated by homogeneous broadening and for cases of Doppler-free excitation with a laser bandwidth within the homogenous linewidth. Our model provides also an adequate description of saturation-curve shapes for partial saturation and inhomogenous broadening. For the case of domination by inhomogeneous broadening and broad-band excitation an empirical equation presented here provides a satisfying description of polarization-spectroscopy-saturation-curve shapes.

The onset of saturation is found to increase with the collisional width. For monochromatic laser excitation and ho-mogenous line broadening the model predicts a dependence of the saturation intensity on quenching and collision rate, which equals that for the similar saturation intensity in degenerate four-wave mixing [26,27].

A polarization-spectroscopy line model has been derived from our generic model. For monochromatic laser excitation and nonsaturating pump intensities, the predicted line shape is Lorentzian cubed while it is pure Lorentzian in the strongly saturated regime. These predictions are in excellent agreement with theoretical investigations of Reichardt and Lucht [11] and experimental investigations of New [37].

The analytical model presented is easily applied to measurements and provides consequently a versatile tool for a detailed investigation of the polarization-spectroscopy-signal-generation process in saturated regimes. Another feature of this model is the possibility to correct measured polarization-spectroscopy signals for fluctuations in the laser intensity even for the intermediate and saturated regime. It gives also an indication on how the analytically cumbersome Liouville equation can be simplified substantially for the case of polarization-spectroscopy. This may also enable the derivation of a practical polarization-spectroscopy theory which is valid for both the saturated and the unsaturated regime.

APPENDIX: CALCULATED FLAME PARAMETERS AND SATURATION INTENSITIES

Values for the absorption saturation intensity were calculated with the balanced cross-rate model presented by Lucht *et al.* [42] and reviewed by Eckbreth ([4], Chaps. 7.2.3 and 7.3.2). As input for this model one needs the temperature and quenching rate in the probe volume. Temperature and mole fractions for OH, CO_2, and H_2O at the center line of the flame were calculated with a detailed one-dimensional kinetic code. No other stable species than CO_2 and H_2O are stated here as the latter were found to be the only entailing a noticeable contribution to the quenching rate, the absorption saturation intensity, and the collisional width. The output of the flame calculation served as input for the calculation of the quenching rate as outlined by Eckbreth ([4], Chap. 7.2.2). The necessary quenching cross sections for this calculations were taken from [43]. The temperature, the chemical composition, the quenching rate, and the resulting saturation intensities are listed in Table I. The collisional widths $\Delta \nu_c$ were

calculated using the listed chemical composition and temperature in Table I together with results reported by Rea *et al.* [44]. The collision rate R_c can be obtained from $\Delta \nu_c$ in s^{-1} with $R_c = 2\pi\Delta\nu_c$. The uncertainty (95% confidence interval) of the cross sections provided in [44] is roughly 40%.

The temperature features an uncertainty of approximately 50% due to incomplete knowledge of input parameters to the kinetic code and due to a simplified radiation model in the latter. The uncertainty of the mole fractions (H_2O and CO_2) is negligible compared to the other sources of uncertainty.

---

[1] C. Wieman and T.W. Hänsch, Phys. Rev. Lett. **36**, 1170 (1976).

[2] R. E. Teets *et al.*, in *Proceedings of the Society of Photo-Optical Instruments and Engineering*, edited by A. H. Zewail (Society of Photo-Optical Instruments and Engineering, Bellingham, WA, 1977), Vol. 113, pp. 80–87.

[3] W. Demtröder, *Laser Spectroscopy* (Springer-Verlag, Berlin, 1996).

[4] A. C. Eckbreth, *Laser Diagnostics for Combustion Temperature and Species* (Overseas Publishers Association, Amsterdam, 1996).

[5] K. Nyholm, R. Maier, C.G. Aminoff, and M. Kaivola, Appl. Opt. **32**, 919 (1993).

[6] K. Nyholm, R. Fritzon, and M. Aldén, Opt. Lett. **18**, 1672 (1993).

[7] K. Nyholm, M. Kaivola, and C. Aminoff, Appl. Phys. B: Lasers Opt. **60**, 5 (1995).

[8] K. Nyholm, R. Fritzon, N. Georgiev, and M. Aldén, Opt. Commun. **114**, 76 (1995).

[9] A. Dreizler, T. Dreier, and J. Wolfrum, J. Mol. Struct. **349**, 285 (1995).

[10] C.F. Kaminski, B. Löfstedt, R. Fritzon, and M. Aldén, Opt. Commun. **129**, 38 (1996).

[11] T.A. Reichardt and R.P. Lucht, J. Chem. Phys. **109**, 5830 (1998).

[12] W.C. Giancola, T.A. Reichardt, and R.P. Lucht, J. Opt. Soc. Am. B **17**, 1781 (2000).

[13] T.A. Reichardt *et al.*, J. Chem. Phys. **113**, 2263 (2000).

[14] T.A. Reichardt, W.C. Giancola, and R.P. Lucht, Appl. Opt. **39**, 2002 (2000).

[15] S. Nakayama, J. Phys. Soc. Jpn. **50**, 609 (1981).

[16] J. Walewski and C. F. Kaminski (unpublished).

[17] P.W. Smith and T. Hänsch, Phys. Rev. Lett. **26**, 740 (1971).

[18] A. Dreizler *et al.*, Chem. Phys. Lett. **240**, 315 (1995).

[19] A.A. Suvernev, A. Dreizler, T. Dreier, and J. Wolfrum, Appl. Phys. B: Lasers Opt. **61**, 421 (1995).

[20] A.A. Suvernev, R. Tadday, and T. Dreier, Phys. Rev. A **58**, 4102 (1998).

[21] V.R. Mironrnko and V.I. Yudson, Opt. Commun. **34**, 397 (1980).

[22] V. Baev, G. Gaida, H. Shroeder, and P.E. Toschek, Opt. Commun. **38**, 309 (1981).

[23] R. L. Ketter and J. S. P. Prawel, *Modern Methods of Engineering Computation* (McGraw-Hill, New York, 1969).

[24] T.A. Reichardt, W.C. Giancola, C.M. Shappert, and R.P. Lucht, Appl. Opt. **38**, 6951 (1999).

[25] T.A. Reichardt and R.P. Lucht, J. Opt. Soc. Am. B **13**, 1107 (1996).

[26] R.L. Abrams and R.C. Lind, Opt. Lett. **2**, 94 (1978).

[27] R.L. Abrams and R.C. Lind, Opt. Lett. **2**, 205 (1978).

[28] R.L. Farrow, D. Rakestraw, and T. Dreier, J. Opt. Soc. Am. B **9**, 1770 (1992).

[29] H.-H. Ritze, V. Stert, and E. Meisel, Opt. Commun. **29**, 51 (1979).

[30] K. Nyholm, M. Kaivola, and C.G. Aminoff, Opt. Commun. **107**, 406 (1994).

[31] S. Nakayama, Phys. Scr. **T70**, 64 (1997).

[32] J. Griffiths and J. Barnard, in *Flame and Combustion*, 3rd ed. (Blackie Academic & Professional, London, 1995).

[33] G.H. Dieke and H.M. Crosswhite, J. Quant. Spectrosc. Radiat. Transf. **2**, 97 (1962).

[34] J. Luque and D. Crosley SRI Report No. MP 96-001, 1996 (unpublished).

[35] J. Luque, LIFBASE—Database and Spectral simulation for diatomic molecules, 1999, http://www.sri.com/psd/lifbase/

[36] D. C. Montgomery, *Design and Analysis of Experiments*, 4th ed. (Wiley, New York, 1997).

[37] M. New, Ph.D. thesis, Wolfson College, Oxford, 1996.

[38] T. Metz, J. Walewski, and C. F. Kaminski, Meas. Sci. Technol. (to be published).

[39] *Lehrbuch der Experimentalphysik*, 9th ed., edited by H. Niedrig (de Gruyter, Berlin, 1993), Vol. 3.

[40] W. Press, B. Flannery, S. Teukolsy, and W. Vetterling, *Numerical Recipes in Pascal* (Cambridge University Press, Cambridge, 1992).

[41] E.H. Piepmeier, Spectrochim. Acta, Part B **27**, 431 (1972).

[42] R.P. Lucht, D.W. Sweeney, and N.M. Laurendeau, Appl. Opt. **19**, 3295 (1980).

[43] N. L. Garland and D. R. Crosley, in the *Twenty-first International Symposium on Combustion* (The Combustion Institute, Pittsburgh, PA, 1986), pp. 1693–1702.

[44] E. Rea, Jr., A. Chang, and R. Hanson, J. Quant. Spectrosc. Radiat. Transf. **41**, 29 (1989).